Supporting Information Appendix for

Carrier Dynamics and the Role of Surface Defects: Designing a Photocatalyst for Gas-Phase CO_2 Reduction

Laura B. Hoch,[1] Paul Szymanski,[2] Kulbir Kaur Ghuman,[3] Le He,[1] Kristine Liao,[1] Qiao Qiao,[4,5] Laura M. Reyes,[1] Yimei Zhu,[4] Mostafa A. El-Sayed,[2] Chandra Veer Singh,[3,6] Geoffrey A. Ozin*[1]*

[1] Department of Chemistry, University of Toronto, 80 St. George St., Rm 326, Toronto, Ontario, M5S 3H6, Canada.

[2] Laser Dynamics Laboratory, School of Chemistry and Biochemistry, Georgia Institute of Technology, 901 Atlantic Dr, Atlanta, Georgia 30332-0400, USA.

[3] Department of Materials Science and Engineering, University of Toronto, 184 College St., Suite 140, Toronto, Ontario M5S 3E4, Canada.

[4] Condensed Matter Physics and Materials Science Department, Brookhaven National Laboratory, Upton, NY, 11973, USA.

[5] Department of Physics, Temple University, Philadelphia, PA, 19122, USA.

[6] Department of Mechanical and Industrial Engineering, University of Toronto, 5 King's College Road, Toronto, Ontario, M5S 3G8, Canada.

* Corresponding Authors: gozin@chem.utoronto.ca, +1 416 487 9556; chandraveer.singh@utoronto.ca, +1 416 946 5211

KEYWORDS Indium oxide, Solar fuels, CO_2 hydrogenation, Transient absorption, Surface defects, Excited state, Frustrated Lewis pair

Supporting Information Appendix

Synthesis of In$_2$O$_{3-x}$(OH)$_y$ nanoparticles:

To prepare the In$_2$O$_{3-x}$(OH)$_y$ nanoparticles, first an amorphous indium hydroxide precursor was synthesized by dissolving indium(III) chloride (3.6 g, 16.2 mmol, Sigma Aldrich, 98%) in a 3:1 solution of anhydrous ethanol (54 ml, Commercial Alcohols) and deionized, Nanopure water (18 ml, resistivity 18.2 MΩ cm). A separate solution of 3:1 mixture of ethanol (54 ml) and ammonium hydroxide (18 mL, Caledon, 28-30 % adjusted to 25 wt% with deionized water) was then rapidly added, resulting in the immediate formation of a white precipitate. The resulting suspension was immediately immersed in a pre-heated oil bath at 80 °C and stirred at a high rate for 10 min. The precipitate was separated via centrifugation and washed 3 times with deionized water. The precipitate was sonicated between washings to ensure adequate removal of any trapped impurities and then dried overnight at 80 °C in a vacuum oven. The dried precursor powder was finely ground with a mortar and pestle, divided into three separate portions, and calcined for 3 hours in air at 250 °C, 350 °C, or 450 °C. Sample films were prepared for photocatalytic testing by drop casting 20 mg of In$_2$O$_{3-x}$(OH)$_y$ nanoparticle powder - suspended via sonication in 3 ml of deionized, Nanopure water - onto 1"x1" binder free borosilicate glass microfiber filters (Whatman, GF/F, 0.7 μm).

Catalysis measurements:

Gas-phase photocatalytic rate measurements were conducted in a custom fabricated 1.5 mL stainless steel batch reactor with a fused silica view port sealed with Viton O-rings. The reactors were evacuated using an Alcatel dry pump prior to being purged with H$_2$ gas (99.9995%) at a flow rate of 6 mL/min for 1 hour. The outlet valve was sealed and the reactors were injected with 1 atm of ^{13}CO$_2$ (99.9 atomic % Sigma Aldrich). The inlet valve was then sealed and the reactors were heated to 150°C. The reactor temperatures were controlled by an OMEGA CN616 6-Zone temperature controller, with a thermocouple placed in contact with the sample. The pressure inside the reactor during reaction was monitored during the reaction using an Omega PX309 pressure transducer. Reactors were irradiated with a 1000 W Hortilux Blue metal halide bulb for a period of 16 hours. Product gases were analyzed by a flame ionization detector (FID) and

thermal conductivity detector (TCD) installed in a SRI-8610 Gas Chromatograph (GC) with a 3'
Mole Sieve 13a and 6' Haysep D column. Isotope product gases were measured using an Agilent
7890A gas chromatographic mass spectrometer (GC-MS) with a 60 m GS-Carbonplot column
fed to the mass spectrometer.

Transient Absorption Spectroscopy Measurements:

Samples films were prepared for measurement by adding the indium oxide powder samples to
deionized water and sonicating. The fine suspension was then drop-cast onto 1-mm thick quartz
substrates, for measurements in air, or onto the inside of 1 of 2 oppositely-facing quartz windows
of a glass photochemical cell, for measurements in other atmospheres. Immediately before TA
experiments, the photochemical cell with sample inside was briefly heated to 100 $^{\circ}$C, allowed to
cool as it was purged vigorously with Ar (99.999%, Airgas), H_2 (99.999%, Airgas), or bone-dry
CO_2 (99.999%, Airgas), then sealed with a Teflon stopcock.

Measurements were carried out with a Helios UV-visible spectrometer (Ultrafast Systems,
Sarasota, Florida, USA). Two different pump wavelengths were used to compare above-optical-
band-gap (318 nm) with near-band-gap (405 nm) excitation. Pump light at 318 nm was obtained
from the fourth harmonic of the signal from a Coherent (Santa Clara, California, USA) OPerA
Solo optical parametric amplifier which was pumped by a Coherent Libra regeneratively-
amplified Ti:sapphire laser (809 nm, 50 fs pulses, 1 kHz repetition rate). The fundamental laser
output was passed through a β-BaB_2O_4 crystal to produce pump light at the second harmonic
wavelength of 405 nm. A broadband probe beam was produced by focusing a small fraction of
the fundamental wavelength into a sapphire or CaF_2 crystal. Both pump and probe were focused
and overlapped on the surface of the substrate. The transmitted probe light was focused into a
fiber-coupled Si array detector with a detection range of 300–907 nm. Scattered pump light was
blocked by a long-pass filter placed before the detector. A rotating mechanical chopper blocked
every other pump pulse with the difference between two consecutive spectra — one with the
pump beam, and one without — yielding the TA signal $\Delta A(t)$, where *t* is the time delay between
pump and probe pulses.

The incident fluence of the pump beam was calculated from the average power, repetition rate,
and $1/e^2$ (Gaussian) radius of the focused laser beam at the sample position. The radius was

measured by the knife-edge method,(13) with a razor blade placed in the Helios sample holder and translated by a Newport (Irvine, California, USA) NSA12 motorized actuator, and the power measured by a calibrated Si photodiode sensor (Newport 818-UV).

Data was analyzed in MATLAB (Mathworks, Natick, Massachusetts, USA) software using the Nelder-Mead simplex algorithm for fitting.(14) Each data set, collected with a single pump wavelength, incident pump fluence, and a series of probe wavelengths (λ), was fit to a sum of exponentials and a constant term (see Results and Discussion for more details). For estimating uncertainties in the parameters, the bootstrap Monte Carlo method was used with 1000 simulated data sets for each experimental data set.(14) For each parameter, the distribution of fit values was analyzed to find the width of the central 68% of the distribution to obtain the standard deviation. The standard deviations are quoted after the "±" in the tables of fit parameters.

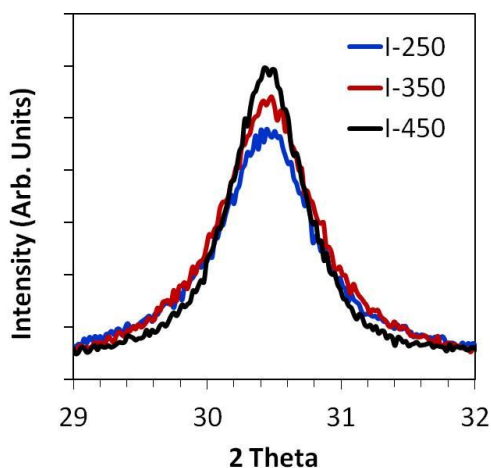*Physical and Optical Characterization of the $In_2O_{3-x}(OH)_y$ samples:*

Figure S1: Zoomed-in view of the (222) reflection of the I-250, I-350, and I-450 samples, which is the most intense peak in the powder X-ray diffraction pattern from figure 2a in the main text. This figure illustrates the peak sharpening as the calcination temperature is increased from 250 °C to 450 °C, indicating an increase in particle size, which is consistent with STEM results illustrated in Figure 1.
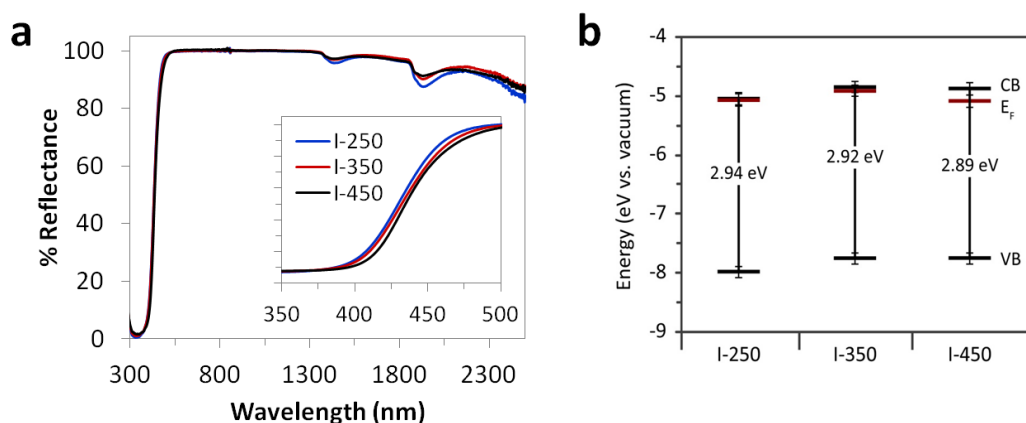
Figure S2. Optical and electronic characterization of the In$_2$O$_{3-x}$(OH)$_y$ samples. (a) UV-Visible-Near-IR absorption spectra. Inset shows the relatively small difference in absorption onset at the band edge between the two samples. (b) Band diagrams for all samples. The valence band (VB) maximum and Fermi level (E$_F$) were measured using XPS. The numbers in between the VB and conduction band (CB) represent the optical band gap for each sample, which was determined by fitting the linear portion of the reflectance spectrum calculate the absorption onset. The CB value represents the mathematical sum of the optical band gap and the VB energy value.

The optical properties of the three samples are shown in Figure S2a and S2b. The diffuse reflectance spectra in Figure S2a indicate that the steady-state absorption of the three samples is very similar. The inset shows that there is a very slight blue-shift in the absorption onset for samples calcined at lower temperatures. However like most metal oxides, the Bohr exciton radius of indium oxide is very small, around 2.4 nm, so it is unlikely that this slight shift is due to the effects of quantum confinement.(1) Fitting the absorption onset using a modified Kubelka-Munk approximation confirms that the band gaps of all samples are very similar (values shown in Figure S2b). The two peaks in the near-IR region of the reflectance spectra centered around 1450 nm and 1925 nm correspond to vibrational overtones and combination modes of hydroxyl groups and surface bound water.(2) The highest contribution of these signals is seen for I-250, which is consistent with the higher concentration of residual hydroxyl groups remaining in the sample after calcination. The other key feature in the reflectance spectra is the gradual increase

in absorbance (i.e. decrease in reflectance) in the near-IR region of the spectrum, which is indicative of conduction electrons within the material. This is consistent with XPS measurements that reveal a high, n-type position of the Fermi-levels relative to the conduction bands (Figure S2b), indicating that there are a significant number of donor defects present in the samples.(3) While the Fermi level of I-450 appears to be slightly lower than the other two samples, which could indicate a decrease in donor states due to the higher calcination temperature, this difference is within the experimental error of the XPS measurements and may not be significant.

Additional Photocatalytic Testing Results:
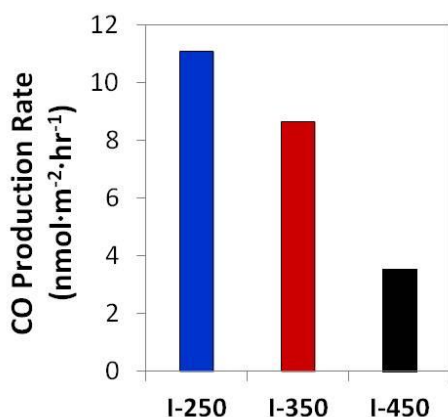
Figure S3: Surface area normalized photocatalytic activity of the $In_2O_{3-x}(OH)_y$ samples under 800 W m^{-2} (0.8 suns) illumination at 150 °C and confirmed using ^{13}C isotope tracing.

Figure S3 presents the surface area normalized photocatalytic activity data for the three $In_2O_{3-x}(OH)_y$ samples. As shown, this trend is very similar to the trend illustrated in Figure 2c in the main text, indicating that the difference in surface area alone is not sufficient to explain the differences in photocatalytic activity.
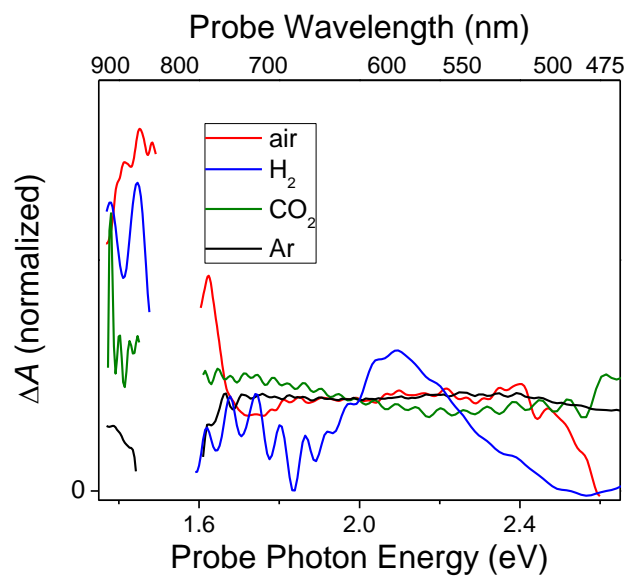
Additional Transient Absorption Results:

Figure S4. Representative TA spectra of I-250 thin films on quartz in air, H_2, CO_2, and Ar atmospheres. In each case, the pump wavelength is 405 nm, the incident pump fluence is 0.7 mJ cm^{-2} (except for 0.45 mJ cm^{-2} in the case of CO_2), and the pump-probe delay is 2 ps. A fresh film was used for each measurement. Data is normalized relative to the signal at 2.0 eV. The data gap centered at ~1.53 eV (809 nm) is due to the strong residual laser fundamental in the probe beam, which led to poor data within this region.
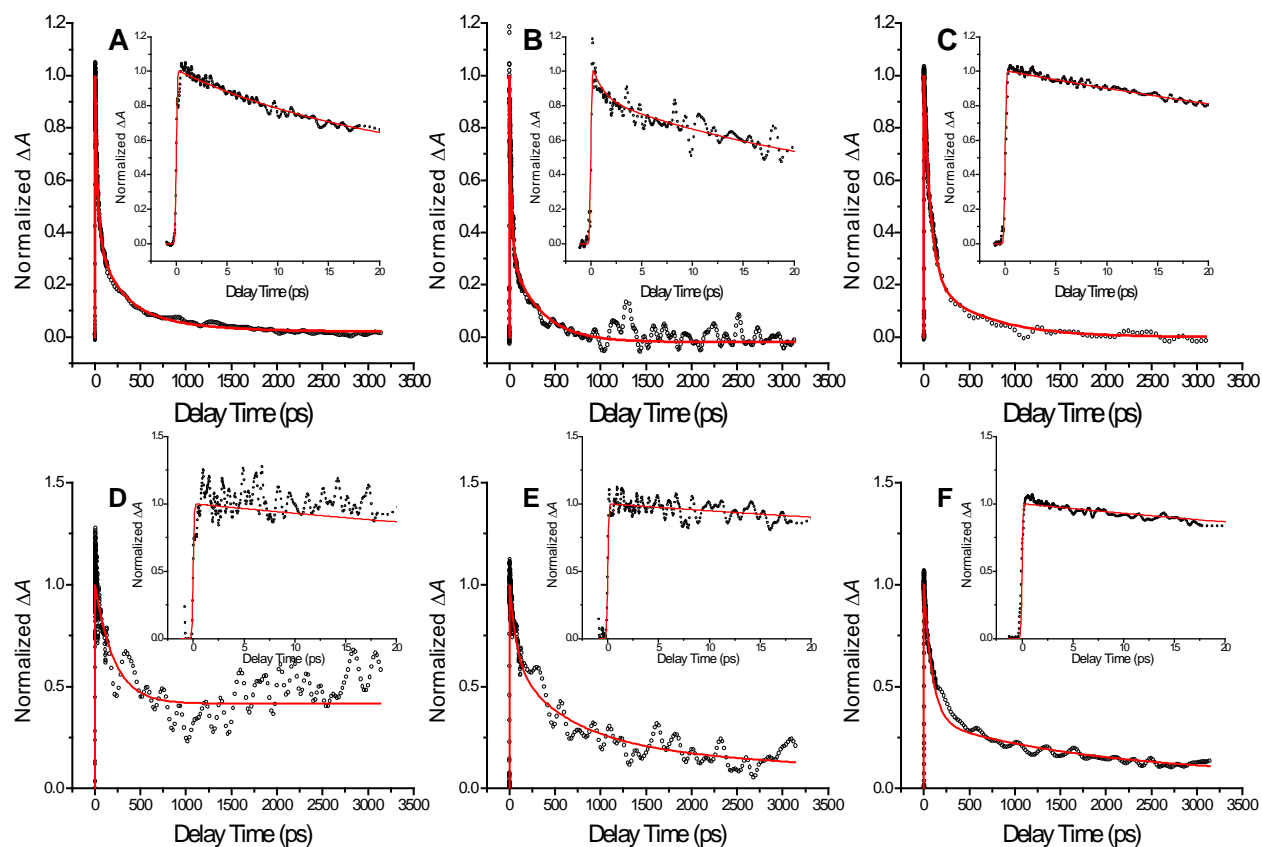
Figure S5. Representative TA data (black circles) and (red lines). The main graphs show the full experimental time window, and the insets show the first 20 ps in each case. For display, the plots have been normalized relative to the maximum value of the fit, and the experimental data was smoothed by a 3-point FFT filter in OriginPro software. The pump wavelength is 405 nm, and measurements were performed in air: A) I-250, 1.33 mJ cm^{-2} incident pump fluence, probed at 534 nm; B) I-350, 1.31 mJ cm^{-2} incident pump fluence, probed at 593 nm; C) I-450, 1.31 mJ cm^{-2} incident pump fluence, probed at 856 nm; D) I-250, 0.202 mJ cm^{-2} incident pump fluence, probed at 521 nm; E) I-250, 0.202 mJ cm^{-2} incident pump fluence, probed at 688 nm; F) I-250, 0.202 mJ cm^{-2} incident pump fluence, probed at 892 nm.
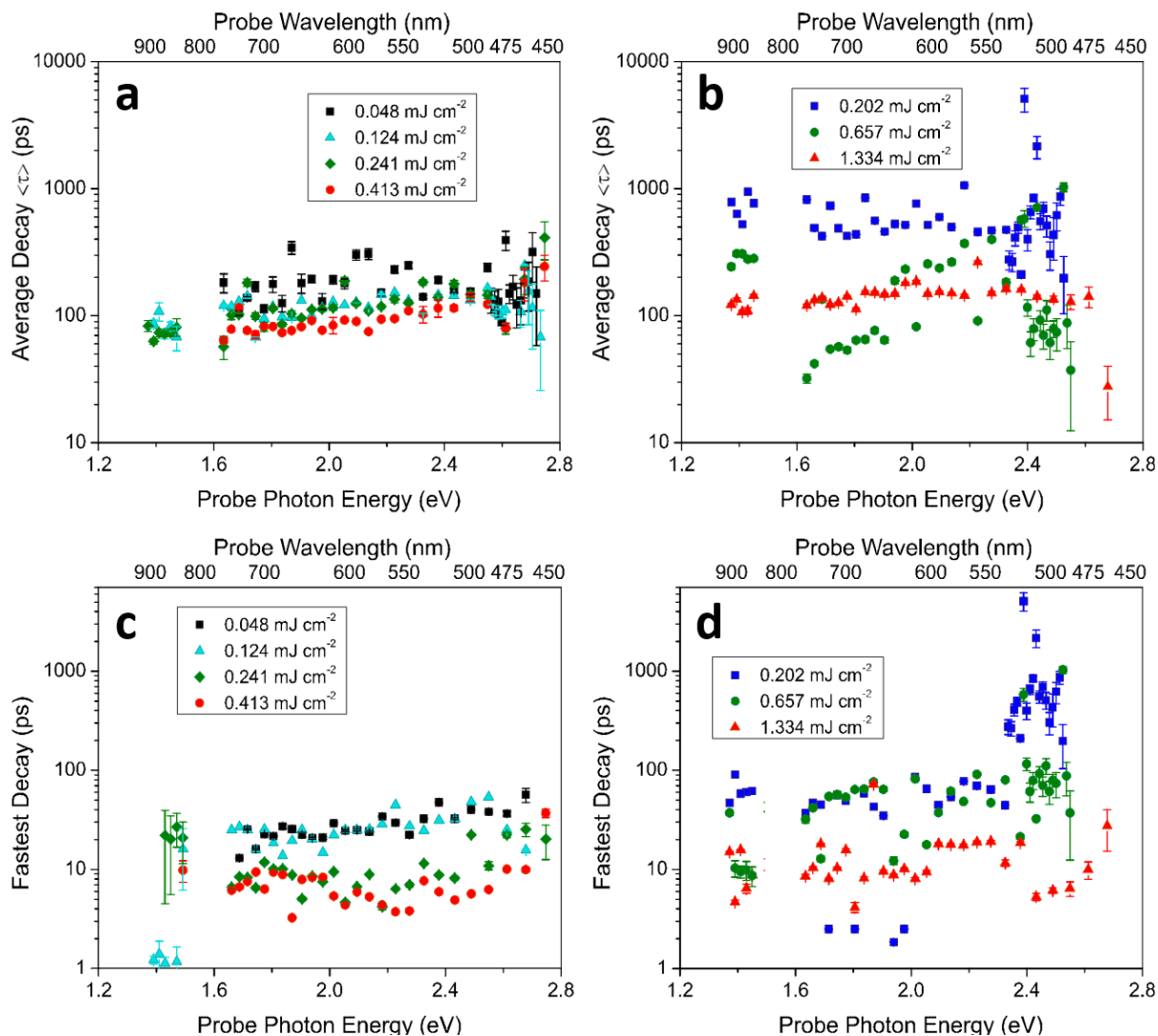
Figure S6. Decay times from the multi-exponential fitting of the TA spectra as a function of probe energy for I-250 at different excitation wavelengths and fluences: amplitude-weighted average time constants observed with (a) 318 nm and (b) 405 nm excitation, and fastest time constants observed with (c) 318 nm and (d) 405 nm excitation.
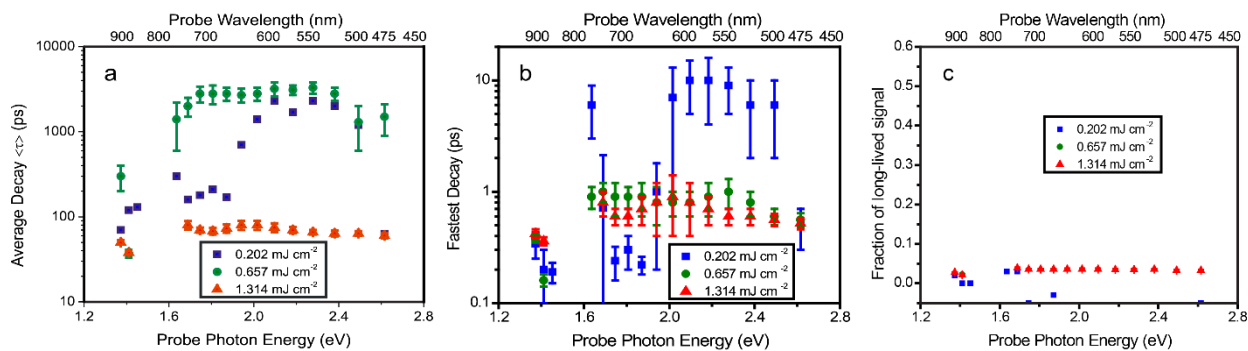
Figure S7. TA results for I-250 in Ar atmosphere, excited at 405 nm as a function of incident pump laser fluence: (a) Average decay time constant $\langle\tau\rangle$, (b) fastest observed decay time constant, (c) fraction of long-lived ($\tau > \sim 10$ ns) signal, equal to A_0. Weak signal at the lowest fluence resulted in greater scatter as a function of wavelength and higher relative standard deviations.
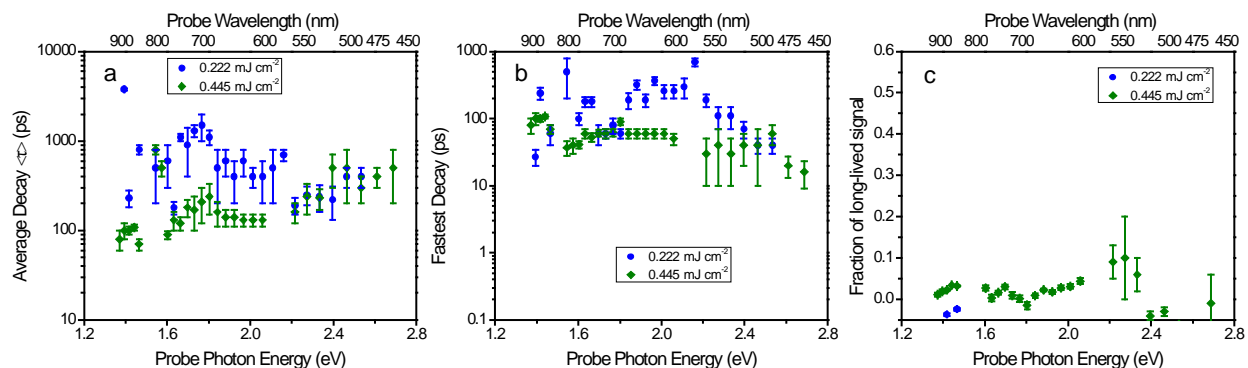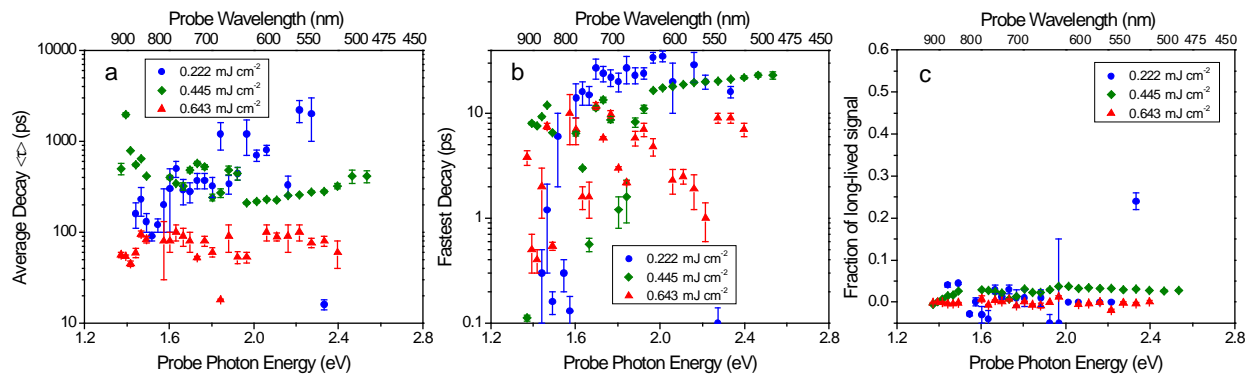

Figure S8. TA results for I-250 in CO_2 atmosphere, excited at 405 nm as a function of incident pump laser fluence: (a) Average decay time constant $\langle\tau\rangle$, (b) fastest observed decay time constant, (c) fraction of long-lived ($\tau > \sim 10$ ns) signal, equal to A_0.

Figure S9. TA results for I-250 in H_2 atmosphere, excited at 405 nm as a function of incident pump laser fluence: (a) Average decay time constant $\langle\tau\rangle$, (b) fastest observed decay time constant, (c) fraction of long-lived ($\tau > \sim 10$ ns) signal, equal to A_0. Weak signal at the lowest fluence resulted in greater scatter as a function of wavelength and higher relative standard deviations.
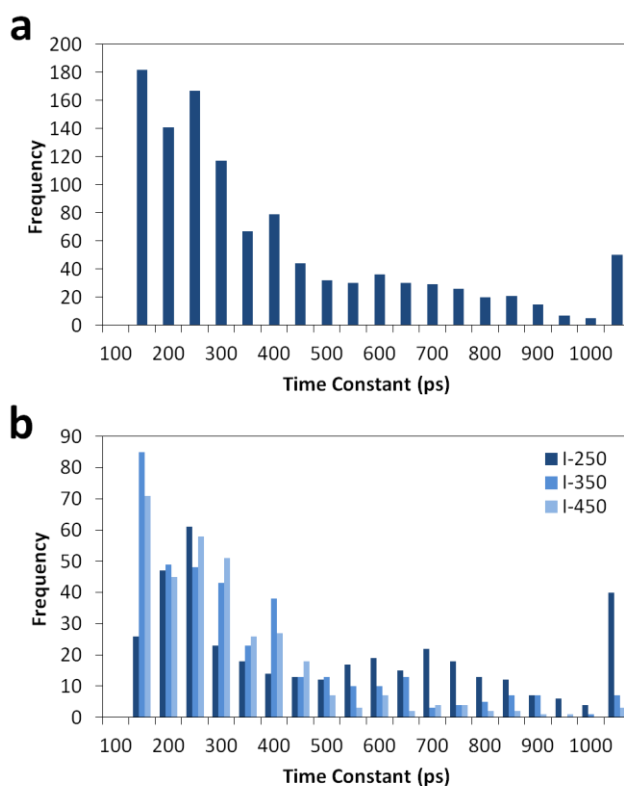
Figure S10. Histogram of frequencies for all time constants greater than 100 ps (a) for all samples measured in air at all wavelengths and fluences and (b) the same data as in plot a, but divided into contributions by sample.

Figure S10a illustrates the distribution of time constants within this range for all samples. Unsurprisingly, there is a greater population of time constants corresponding to faster processes, which is likely due to the many relaxation pathways possible within such highly defected materials. Figure S10b shows the relative contribution from each of the three $In_2O_{3-x}(OH)_y$ samples. While the distributions for I-350 and I-450 are relatively similar, with much greater number of time constants corresponding to faster decay processes, I-250 has a substantially greater population of time constants corresponding to longer relaxation processes.
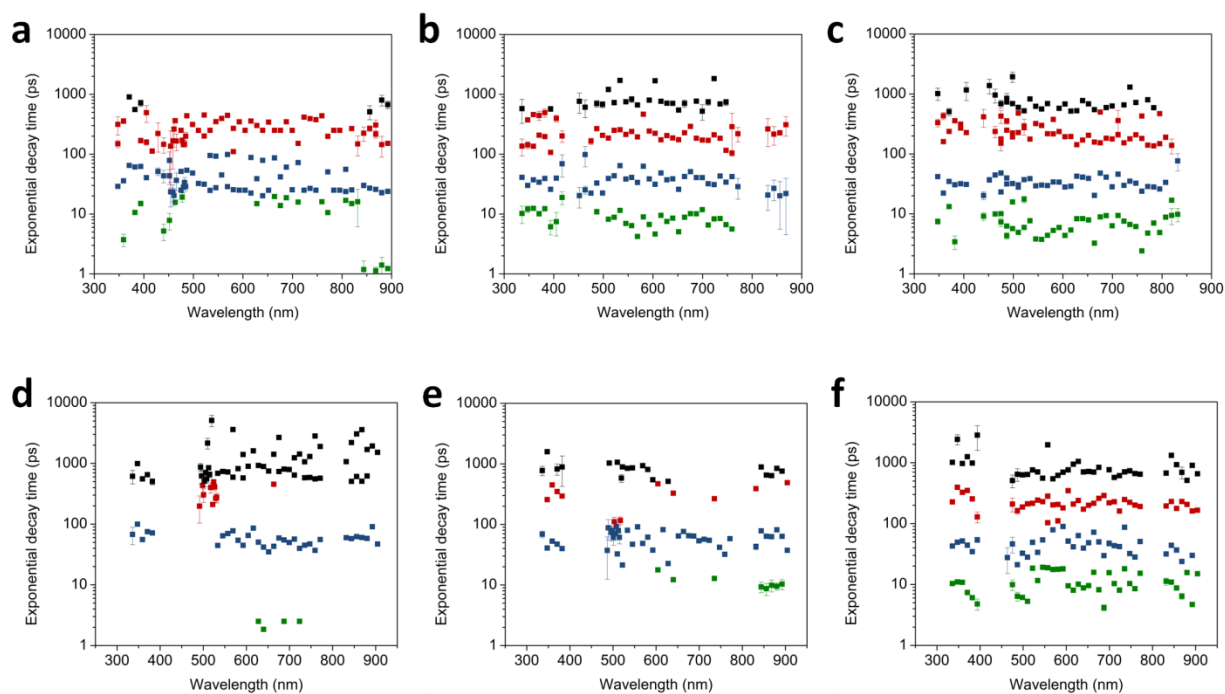
Figure S11. Time constants from the multi-exponential decay fitting of the transient absorption spectra as a function of wavelength for I-250 in air at different excitation wavelengths and fluences (a) 318 nm excitation, 0.090 mJ cm^{-2} (UV) and 0.124 mJ cm^{-2} (Vis/NIR). (b) 318 nm excitation, 0.241 mJ cm^{-2}. (c) 318 nm excitation, 0.413 mJ cm^{-2}. (d) 405 nm excitation, 0.202 mJ cm^{-2}. (e) 405 nm excitation, 0.657 mJ cm^{-2}. (f) 405 nm excitation, 1.334 mJ cm^{-2}. The time constants have been grouped into four categories: $\tau < 20$ ps (green squares), $20 < \tau < 100$ ps (blue squares), $100 < \tau < 500$ ps (red squares), and $\tau > 500$ ps (black squares).
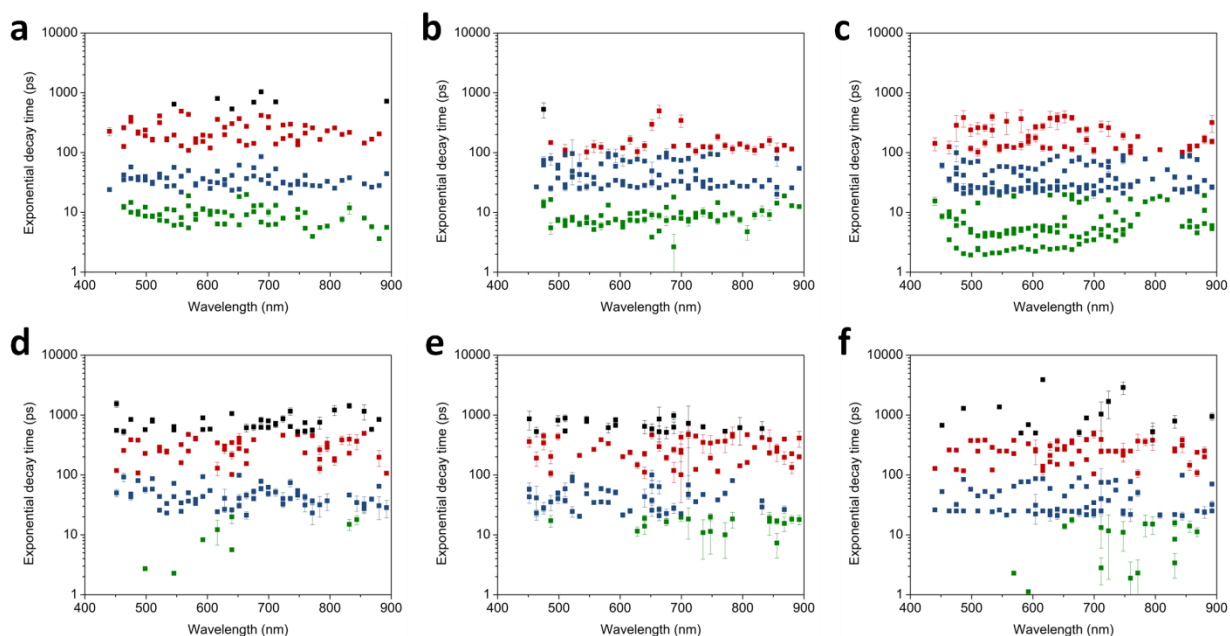
Figure S12. Time constants from the multi-exponential decay fitting of the transient absorption spectra as a function of wavelength for I-350 in air at different excitation wavelengths and intensities (a) 318 nm excitation, 0.124 mJ cm^{-2}. (b) 318 nm excitation, 0.241 mJ cm^{-2}. (c) 318 nm excitation, 0.413 mJ cm^{-2}. (d) 405 nm excitation, 0.657 mJ cm^{-2}. (e) 405 nm excitation, 0.960 mJ cm^{-2}. (f) 405 nm excitation, 1.314 mJ cm^{-2}. The time constants have been roughly grouped into four categories: $\tau < 20$ ps (green squares), $20 < \tau < 100$ ps (blue squares), $100 < \tau < 500$ ps (red squares), and $\tau > 500$ ps (black squares).
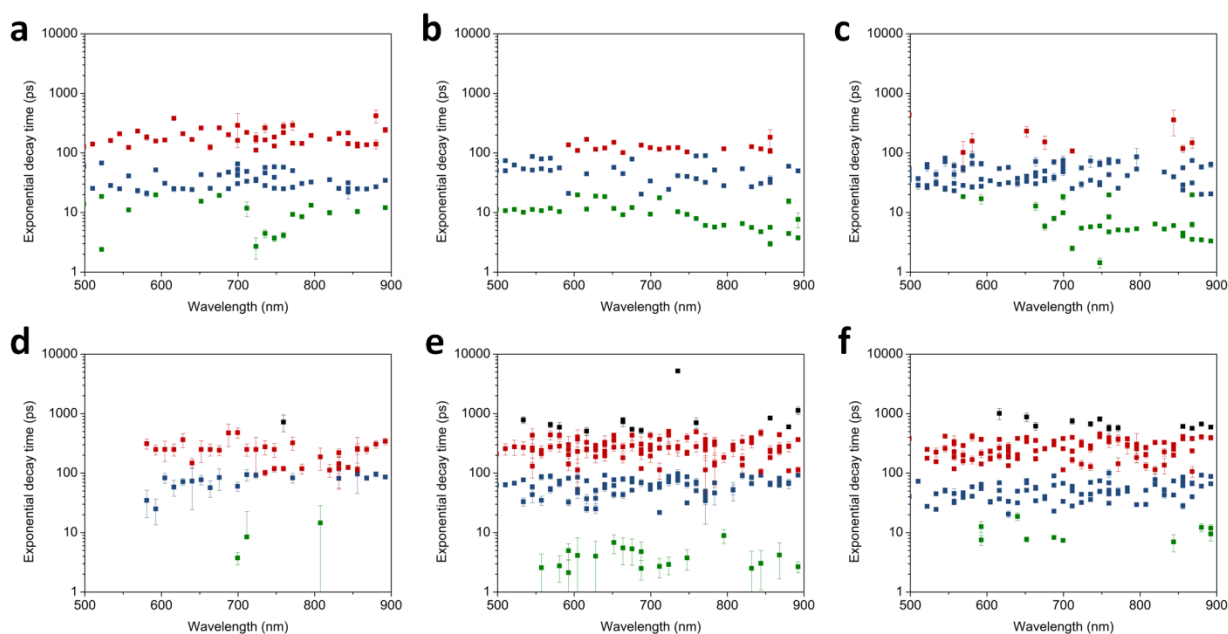
Figure S13. Time constants from the multi-exponential decay fitting of the transient absorption spectra as a function of wavelength for I-450 in air at different excitation wavelengths and intensities (a) 318 nm excitation, 0.124 mJ cm^{-2}. (b) 318 nm excitation, 0.241 mJ cm^{-2}. (c) 318 nm excitation, 0.413 mJ cm^{-2}. (d) 405 nm excitation, 0.202 mJ cm^{-2}. (e) 405 nm excitation, 0.657 mJ cm^{-2}. (f) 405 nm excitation, 1.314 mJ cm^{-2}. The time constants have been roughly grouped into four categories: $\tau < 20$ ps (green squares), $20 < \tau < 100$ ps (blue squares), $100 < \tau < 500$ ps (red squares), and $\tau > 500$ ps (black squares).
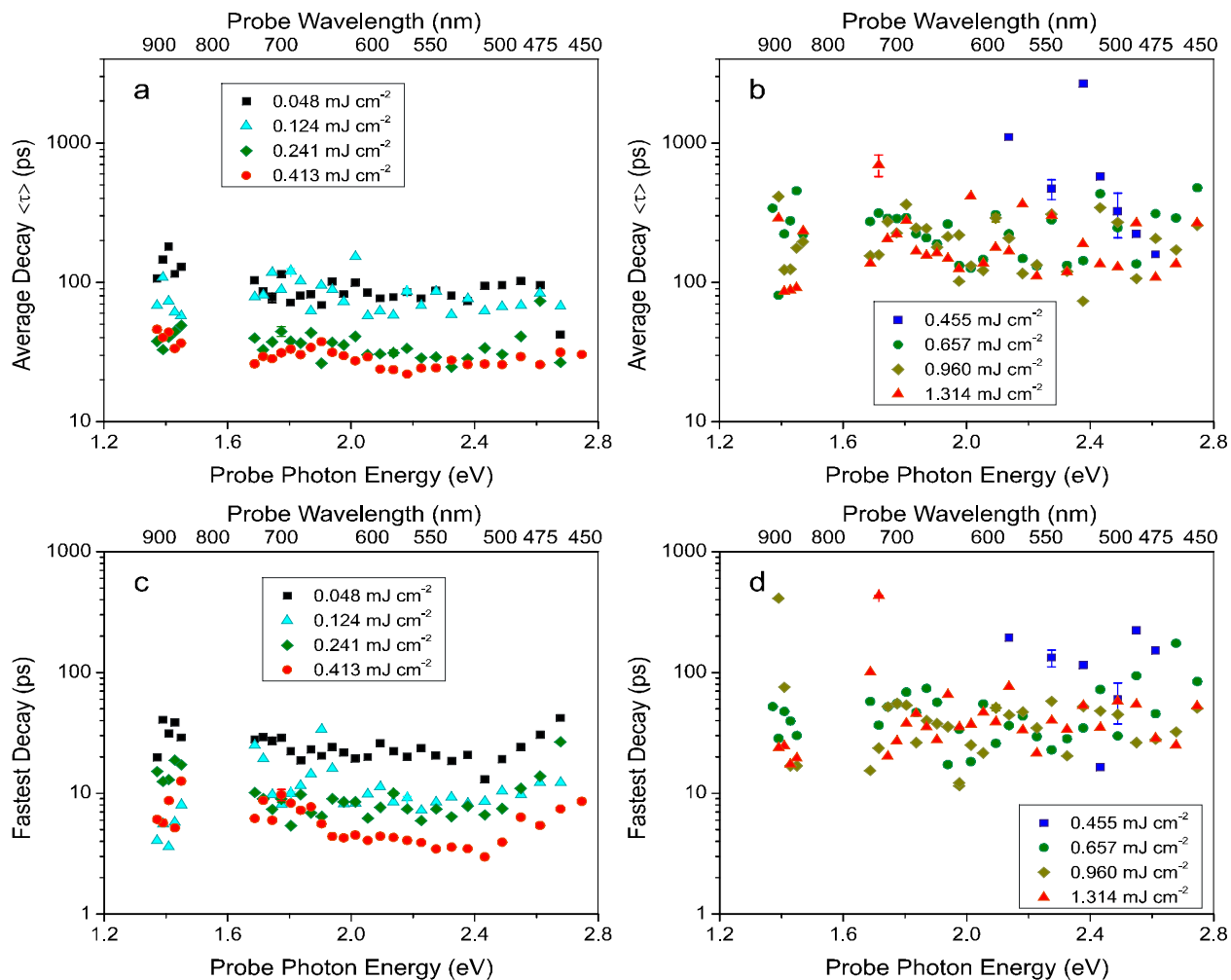
Figure S14. Decay times from the multi-exponential fitting of the TA spectra as a function of probe energy for I-350 in air at different excitation wavelengths and fluences: amplitude-weighted average time constants observed with (a) 318 nm and (b) 405 nm excitation, and fastest time constants observed with (c) 318 nm and (d) 405 nm excitation.

Figure S15. Decay times from the multi-exponential fitting of the TA spectra as a function of probe energy for I-450 in air at different excitation wavelengths and fluences: amplitude-weighted average time constants observed with (a) 318 nm and (b) 405 nm excitation, and fastest time constants observed with (c) 318 nm and (d) 405 nm excitation.
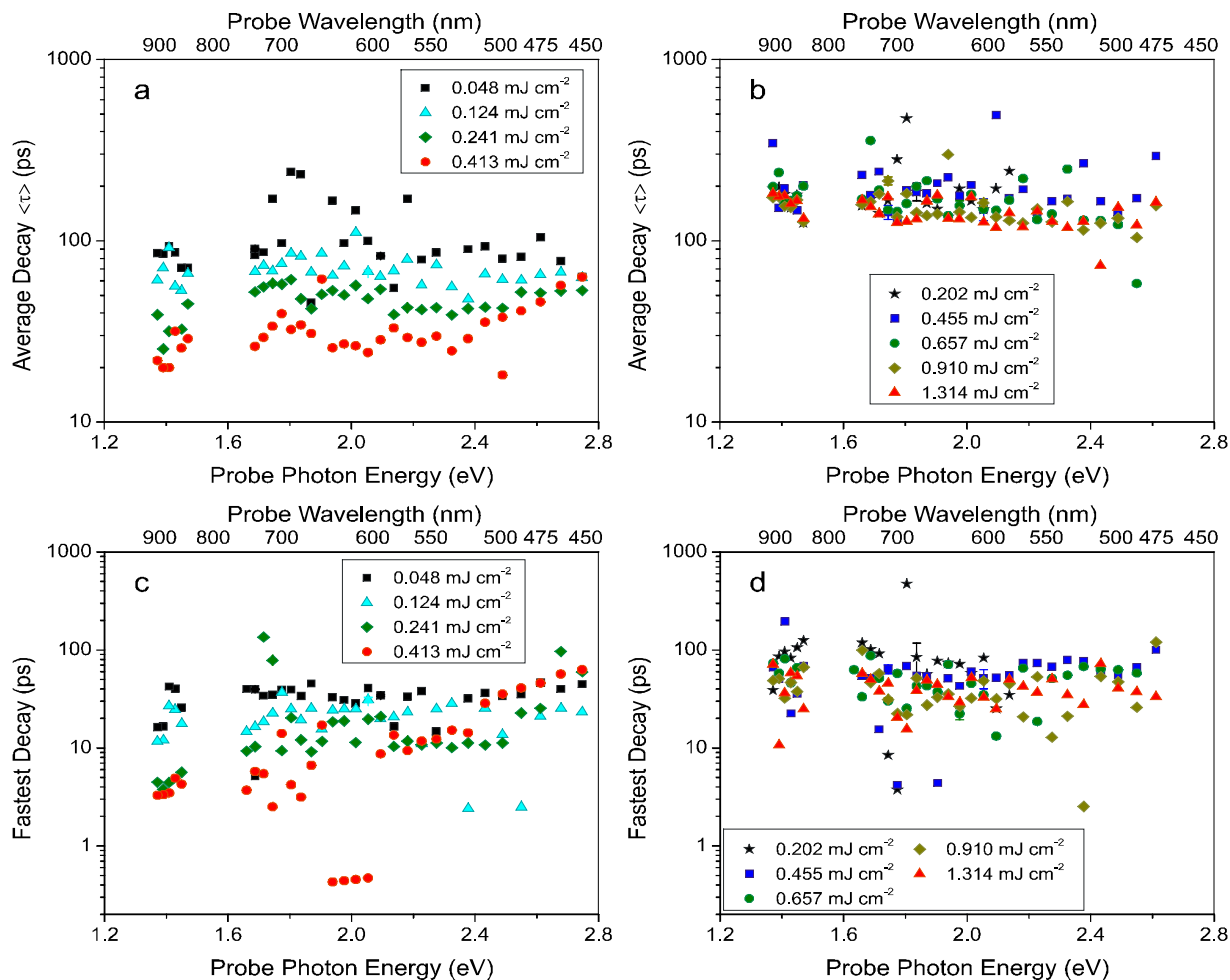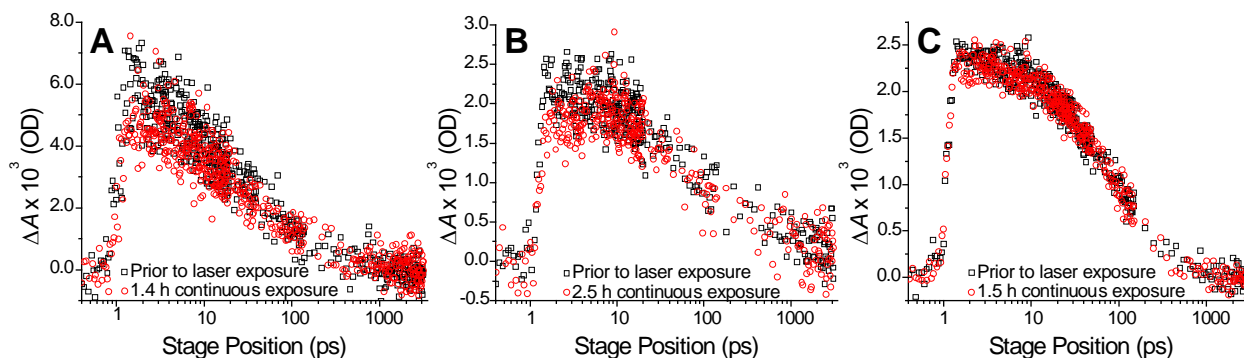
Figure S16. Representative raw TA traces showing the lack of effects of long-term laser exposure on $In_2O_{3-x}(OH)_y$ nanoparticle carrier dynamics: A) I-250 probed at 534 nm, B) I-350 probed at 593 nm, C) I-450 probed at 856 nm. Different probe wavelengths are shown to present a diverse range of measurements, using the best available data in each case. The open black squares represent data prior to any laser exposure and the open red circles represent after continuous laser exposure. The nanoparticles were dropcast onto quartz substrates and measured in air. The nanoparticle films were irradiated continuously with 405 nm laser pulses (50 fs, 500 Hz) at an incident fluence of 1.32 ± 0.01 mJ cm^{-2} without translating the sample or the laser beams for 1.4 - 2.5 h, as specified in each graph. For clarity, the traces are shown using log-10 time axes with the arrival of the pump pulse at a stage position of ~1 ps.
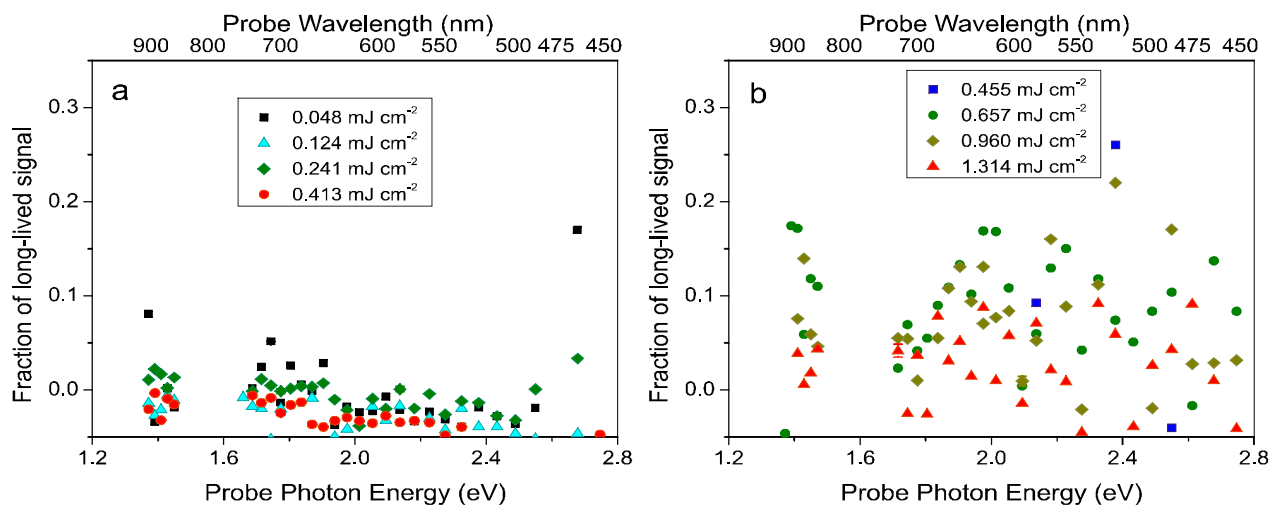
Figure S17. Fraction of long-lived signal ($\tau > \sim 10$ ns), equal to A_0, at different pump fluences for I-350 in air excited with (a) 318 nm light and (b) 405 nm light.

Figure S18. Fraction of long-lived signal ($\tau > \sim 10$ ns), equal to A_0, at different pump fluences for I-450 in air excited with (a) 318 nm light and (b) 405 nm light.
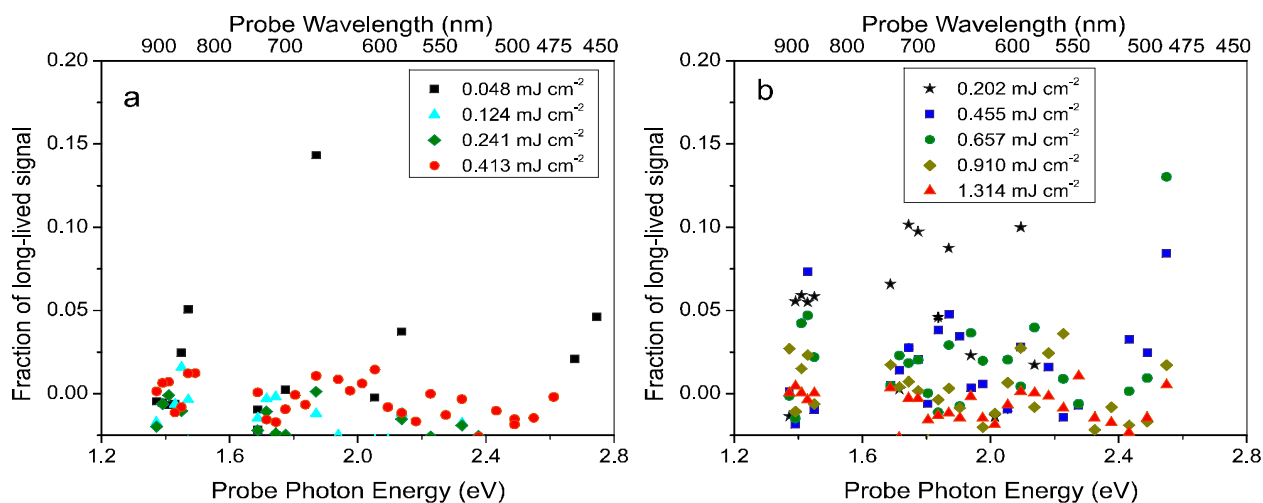
Additional Computational Details:

For calculating the electronic properties plane wave DFT implemented in Quantum ESPRESSO code(4) is used. Electron exchange and correlation was treated using the hybrid HSE06 approach(5, 6) in which 25% of exact nonlocal Hartree-Fock exchange is added to the generalized gradient Perdew-Burke-Ernzerhof functional(7) and a screening of $\omega = 0.11$ Bohr is applied to partition the Coulomb potential into short- and long-range terms. Due to the large system size of the In_2O_3 surfaces and the computational expense of the approach for large system sizes, non-spin polarized calculations were performed. The kinetic energy cut-offs of 40 and 160 Ry were used for the smooth part of the electronic wavefunctions and augmented electron density, respectively. The self-consistent field convergence criterion was set to 1×10^{-5} Ry per Bohr. The structures were relaxed using a conjugate gradient minimization algorithm until the magnitude of residual Hellman-Feynman force on each atom was less than 1×10^{-2} Ry per Bohr for surfaces and 1×10^{-3} Ry per Bohr for bulk In_2O_3. Brillouin zone integrations were performed using a Monkhorst-Pack(8) grid of $2\times2\times2$ k points for the bulk supercell and $2\times1\times2$ for the (111) pristine and defected In_2O_3 surfaces studied. The energy bands are computed only at a small number of k points, due to the numerical costs of the HSE06-DFT approach. A conventional Gaussian smearing of 0.009 Ry was utilized.

To compare the band structure of surfaces with bulk In_2O_3, we modelled a cubic unit cell of bulk In_2O_3, shown in Fig. S19. It has a lattice parameter of 1.0117 nm and contains 80 atoms. Each In atom is six-fold coordinated to neighboring O atoms and each O atom has a tetrahedral coordination to four In neighbors. Fig. S19b shows the total DOS with PDOS for the s, p and d electrons of In atoms and p electrons of O atoms for bulk In_2O_3. In bulk In_2O_3 the valence band is dominated by O 2p derived states, with a lower valence band peak and the conduction band states dominated by In 5s. Additional hybridization of In 4d and 5p states in the valence band is also evident. At this level of theory, the band gap of bulk In_2O_3 was found to be 3.1 eV (see Figure S19) which is consistent with previous analysis.(9, 10) This shows that with the HSE06-DFT technique no further *a posteriori* band gap correction is necessary for a qualitative analysis and that we can use this approach to give reliable estimates for fundamental gaps and electronic structures of pristine and defected In_2O_3 surfaces.
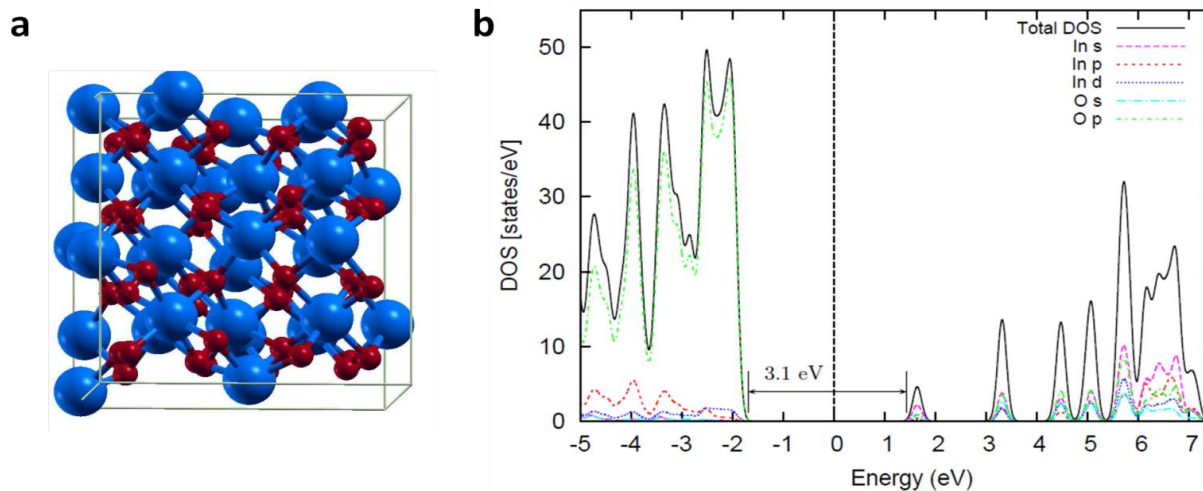
Figure S19. (a) DFT model of bulk In_2O_3 in the ground state. The atomic colors are as follows: blue (In), white (H), and red (O). (b) The total DOS and projected DOS on the s, p and d orbitals of In atoms and s and p orbitals of O atoms for bulk In_2O_3 model. The zero energy value is set at the Fermi level, represented by the vertical dashed line.

To model In_2O_3 surfaces, the (111) surface was chosen based on experimental evidence from our previous work.(11) Notably, this surface is also the most abundant crystal face at thermodynamic equilibrium.(12) In order to examine how O_v and OH defects affect the electronic properties, we created 4 different indium oxide (111) surfaces: a pristine, defect-free indium oxide surface (In_2O_3), a surface containing only an O_v defect (In_2O_{3-x}), a surface containing only an OH defect ($In_2O_3(OH)_y$), and a surface containing both O_v and OH defects ($In_2O_{3-x}(OH)_y$). The optimized DFT models of these surfaces are shown in Figure S20.

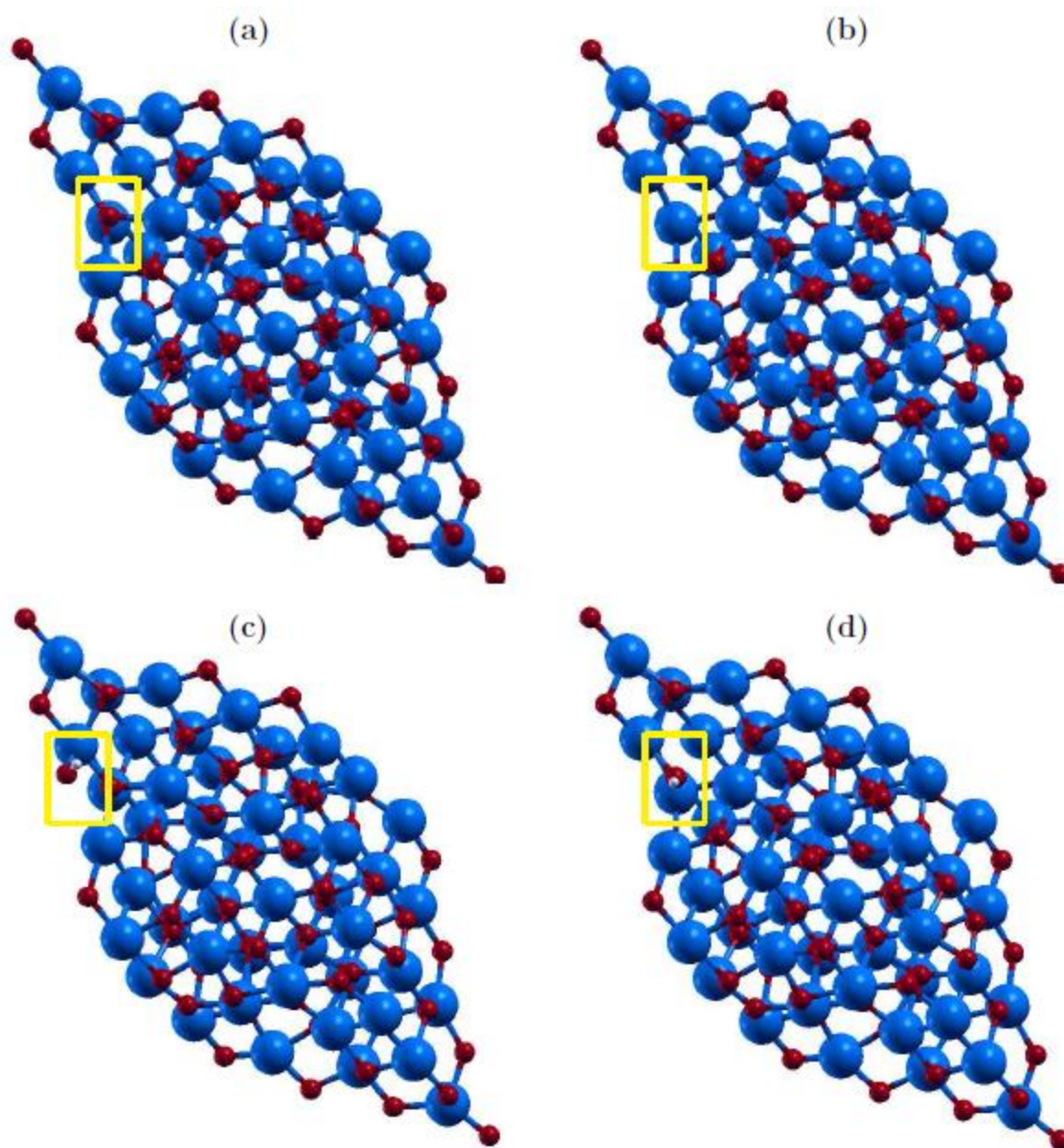**Figure S20.** The optimized DFT models of (a) (111) pristine In_2O_3 surface, (b) (111) In_2O_{3-x} surface with only an O_v defect, (c) (111) $In_2O_3(OH)_y$ surface with only an OH defect, and (d) (111) $In_2O_{3-x}(OH)_y$ surface with both an O_v and OH defects. The site where defects were created is highlighted with yellow box in all the surfaces. The atomic colors are as follows: blue (In), white (H), and red (O).

References:

1. Shao D, Qin L, Sawyer S (2013) Optical properties of polyvinyl alcohol (PVA) coated In2O3 nanoparticles. *Opt Mater (Amst)* 35(3):563–566.

2. Burns DA, Ciurczak EW eds. (2008) *Handbook of Near-Infrared Analysis* (CRC Press, Taylor and Francis Group, Boca Raton, FL). 3rd Ed.

3. King PDC, Veal TD (2011) Conductivity in transparent oxide semiconductors. *J Phys Condens Matter* 23(33):334214.

4. Giannozzi P, et al. (2009) QUANTUM ESPRESSO: a modular and open-source software project for quantum simulations of materials. *J Phys Condens Matter* 21(39):395502.

5. Heyd J, Scuseria GE, Ernzerhof M (2003) Hybrid functionals based on a screened Coulomb potential. *J Chem Phys* 118:8207 –8215.

6. Heyd J, Scuseria GE, Ernzerhof M (2006) Erratum: "Hybrid functionals based on a screened Coulomb potential" [J. Chem. Phys. 118, 8207 (2003)]. *J Chem Phys* 124(21):219906.

7. Perdew JP, Burke K, Ernzerhof M (1996) Generalized gradient approximation made simple. *Phys Rev Lett* 77(18):3865–3868.

8. Monkhorst HJ, Pack JD (1976) Special points for Brillouin-zone integrations. *Phys Rev B* 13:5188.

9. Fuchs F, Bechstedt F (2008) Indium-oxide polymorphs from first principles: Quasiparticle electronic states. *Phys Rev B* 77(15):155107.

10. Vidal J, Trani F, Bruneval F, Marques MAL, Botti S (2010) Effects of electronic and lattice polarization on the band structure of delafossite transparent conductive oxides. *Phys Rev Lett* 104(13):136401.

11. Ghuman KK, et al. (2015) Illuminating CO2 reduction on frustrated Lewis pair surfaces: investigating the role of surface hydroxides and oxygen vacancies on nanocrystalline In2O3−x(OH)y. *Phys Chem Chem Phys* 17:14623–14635.

12. Zhang KHL, Walsh A, Catlow CRA, Lazarov VK, Egdell RG (2010) Surface Energies Control the Self-Organization of Oriented In2O3 Nanostructures on Cubic Zirconia. *Nano Lett* 10(9):3740–3746.

13. Skinner DR, Whitcher RE (1972) Measurement of the radius of a high-power laser beam near the focus of a lens. J Phys E 5:237.

14. Press WH, Teukolsky SA, Vetterling WT, Flannery BP (1992) *Numerical Recipes in C: The Art of Scientific Computing* (Cambridge University Press: New York). 2nd ed.